2B.3 AN IMPROVED BULK AIR-SEA SURFACE FLUX ALGORITHM, INCLUDING SPRAY-MEDIATED TRANSFER

Edgar L Andreas[1*], Larry Mahrt[2], and Dean Vickers[3]

[1]NorthWest Research Associates, Inc.; Lebanon, New Hampshire
[2]NorthWest Research Associates, Inc.; Corvallis, Oregon
[3]College of Earth, Ocean, and Atmospheric Sciences, Oregon State University; Corvallis, Oregon

1. INTRODUCTION

Heat and moisture can cross the air-sea interface by two routes. The *interfacial* route, which is controlled by molecular processes right at the air-sea interface, is the one implicitly treated in virtually all turbulent air-sea bulk flux algorithms. The *spray* route, in which transfer is controlled by microphysical processes around sea spray droplets, becomes significant at modest wind speeds of 10–13 m s^{-1}.

Andreas et al. (2008) published our first publicly released version of a bulk air-sea flux algorithm that explicitly treats both the interfacial and spray routes for the air-sea sensible and latent heat fluxes. Andreas (2010) later added comparable parameterizations for the enthalpy, salt, and freshwater fluxes. These two algorithms were denoted, respectively, Version 3.2 and Version 3.4.

Here, we introduce Version 4.0 of this bulk flux algorithm. This version improves on previous versions in two significant ways. In all previous versions, we built the interfacial flux algorithm on the COARE Version 2.6 algorithm (Fairall et al. 1996; see Perrie et al. 2005; Andreas et al. 2008). As such, it obtained a drag coefficient from an aerodynamic roughness length, z_0, which it modeled as a smooth blending of the Charnock relation and an aerodynamically smooth tail in low winds (Smith 1988). Our previous versions also included the COARE gustiness parameterization in unstable stratification and a windless term in stable stratification (from Jordan et al. 1999; Andreas et al. 2008). Both of these parameterizations prevented the surface stress and the scalar fluxes from going to zero when the vector-averaged wind speed was zero.

In Version 4.0, however, we introduce a totally new drag relation (Andreas et al. 2012) that naturally provides a non-zero surface stress even at zero average wind speed and has better properties than the Charnock relation when extrapolated beyond winds of 30 m s^{-1}. Hence, from Version 4.0, we can eliminate the gustiness and windless terms at low wind speed and can reliably extrapolate our algorithm to hurricane-strength winds, where the Charnock relation had previously predicted too much surface drag and, thus, too much dissipation to sustain modeled hurricanes.

The second significant improvement in Version 4.0 is that we have validated and tuned it with 10 times as much data as used in deriving previous versions.

With this enhanced validation for wind speeds up to almost 25 m s^{-1}, because both the interfacial and spray flux algorithms are theoretically based, and since the new drag relation is consistent with theory for wind speeds up to at least 70 m s^{-1}, this new flux algorithm can be extrapolated to hurricane-strength winds. Although forecasts of hurricane track have improved dramatically in the last 15 years, forecasts of hurricane intensity have improved little (e.g., Rogers et al. 2013). Because air-sea exchange is generally believed to control hurricane intensity (e.g., Montgomery et al. 2010; Lee and Chen 2012), the improved predictions of air-sea fluxes that our algorithm promises may provide insights into this difficult problem of predicting hurricane intensity.

2. FLUX CALCULATIONS

2.1. General Outline

As with most flux algorithms, ours provides the "surface" fluxes of momentum (τ, also called the surface stress), latent heat (H_L), and sensible heat (H_s):

[*]*Corresponding author address:* Dr. Edgar L Andreas, NorthWest Research Associates, Inc., 25 Eagle Ridge, Lebanon, NH 03766-1900; e-mail: eandreas@nwra.com.

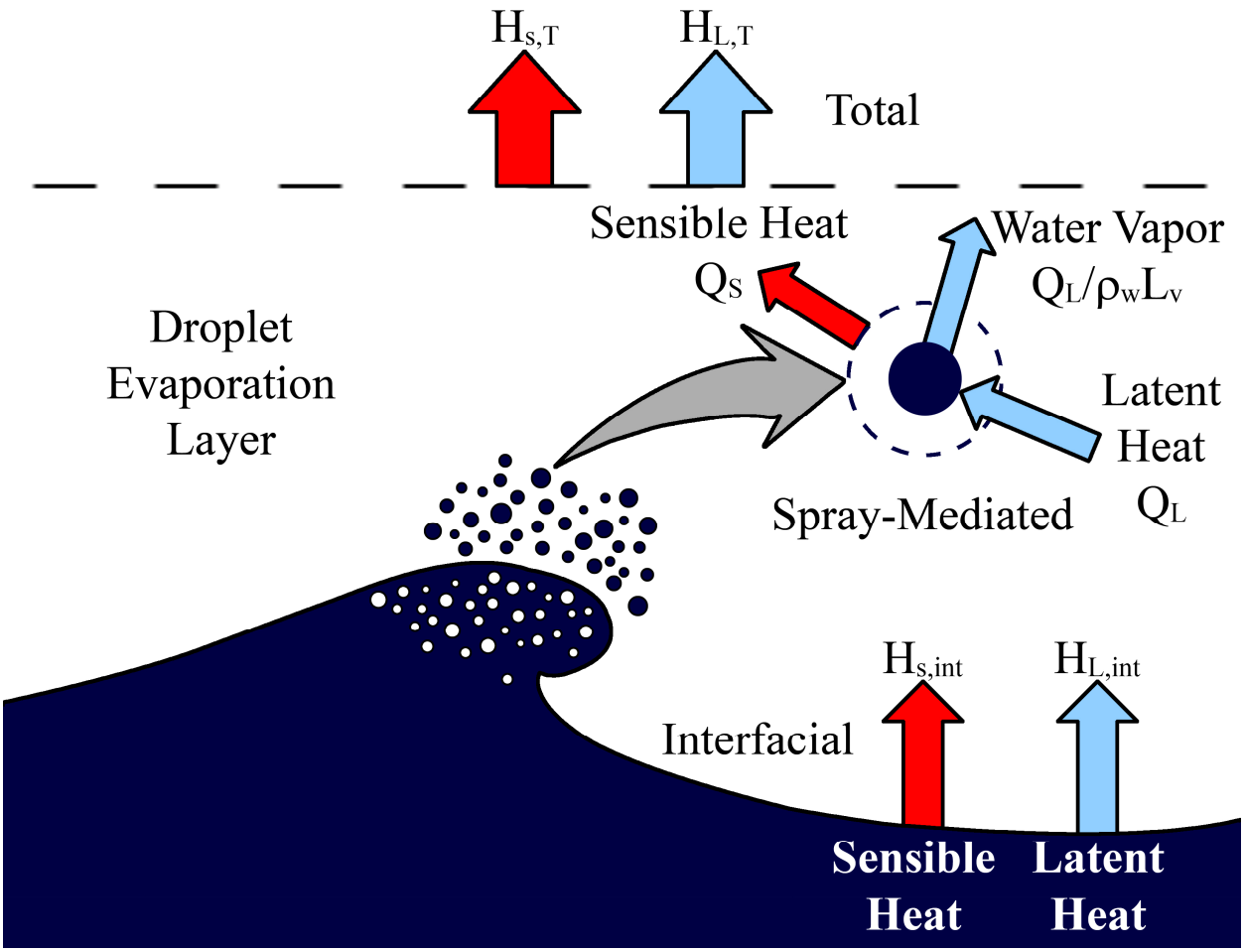

FIG. 1. Processes in the droplet evaporation layer. Air and sea are always exchanging sensible ($H_{s,int}$) and latent ($H_{L,int}$) heat right at the interface. Both fluxes can go in either direction depending on the local air-sea temperature and humidity differences. The labeled circles depict an individual spray droplet. This droplet cools rapidly, thereby giving up sensible heat. Its evaporation yields water vapor but extracts latent heat from the air. Q_L and Q_S are the latent and sensible heat fluxes associated with this single droplet. The interfacial and spray fluxes combine to give the total sensible ($H_{s,T}$) and latent ($H_{L,T}$) heat fluxes coming out the top of the droplet evaporation layer.

$$\tau \equiv \rho_a u_*^2 = \left[f(U_{N10}) \right]^2, \qquad (2.1a)$$

$$H_{L,T} = H_{L,int} + H_{L,sp}, \qquad (2.1b)$$

$$H_{s,T} = H_{s,int} + H_{s,sp}. \qquad (2.1c)$$

Equation (2.1a) is based on our new drag relation, which we describe in the next section. In it, ρ_a is the density of moist air; f is a function of U_{N10}, the 10-m wind speed for neutral stability; and it also defines the friction velocity, u_*.

Figure 1 depicts our conceptual model of the interfacial and spray processes represented in (2.1b) and (2.1c). The ocean and atmosphere are always exchanging latent and sensible heat right at the interface ($H_{L,int}$ and $H_{s,int}$) because of air-sea differences in humidity and temperature, respectively.

When spray is present, the droplets also exchange heat and water vapor with the near-surface air. Spray droplets cool rapidly to an equilibrium temperature that is almost always lower than the local air temperature (Andreas 1995). Through this cooling, the droplets give up sensible heat to the air. In a much slower process, the droplets also give up water vapor by

evaporating (Andreas 1990). Because the droplets are now relatively cool, however, the latent heat for this evaporation must come from the air. As a consequence, this evaporation enhances the interfacial flux of water vapor but cools the near-surface atmosphere, thereby offsetting some of the sensible heating contributed when the droplets initially cooled.

These spray-mediated processes occur over a range of droplet radii that is 1.6 to 500 μm in our current analysis. Each droplet size has different time scales for its exchanges of sensible and latent heat. To get the spray-mediated fluxes in (2.1b) and (2.1c), $H_{L,sp}$ and $H_{s,sp}$, we must combine individual contributions with knowledge of how many droplets are produced and integrate over all radii. We describe that process shortly.

This spray-mediated transfer occurs in a near-surface droplet evaporation layer (Figure 1) that is nominally one significant wave height thick (Andreas et al. 1995; Van Eijk et al. 2001). Hence, the so-called surface fluxes in (2.1b) and (2.1c) are what we denote as the total fluxes ($H_{L,T}$ and $H_{s,T}$) that come out the top of the droplet evaporation layer. These would serve as the lower flux boundary conditions in atmospheric models and be applied at the lowest modeling node. Similarly, we assume that the measured latent and sensible heat fluxes that we use to validate and tune our algorithm were obtained above the droplet evaporation layer and therefore represent $H_{L,T}$ and $H_{s,T}$.

2.2. Drag Relation

Andreas et al. (2012) analyzed over 5600 eddy-covariance measurements of the air-sea surface stress from ships, platforms, and aircraft. This analysis confirmed the observations by Foreman and Emeis (2010) that u_* is a linear function of U_{N10}, the 10-m wind speed at neutral stability, in aerodynamically rough flow over the ocean (cf. Edson et al. 2013).

Andreas et al. (2012) also obtained a linear relation between u_* and U_{N10} for aerodynamically smooth flow and were, therefore, able to connect these two straight-line regions with a hyperbola that predicts u_* from U_{N10} for all wind speeds and is a continuous and differentiable function. That hyperbola, which is the $f(U_{N10})$ function is (2.1a), is

$$u_* = 0.239 + 0.0433 \bullet \left\{ (U_{N10} - 8.271) + \left[0.120 (U_{N10} - 8.271)^2 + 0.181 \right]^{1/2} \right\}. \quad (2.2)$$

Here, both u_* and U_{N10} are in m s^{-1}.

Figure 2 shows (2.2) and the data that Andreas et al. (2012) used in deriving it. The figure also shows theoretical results from Moon et al. (2007) and Mueller and Veron (2009a). Both of these theoretical studies extended to wind speeds of at least 60 m s^{-1}, as depicted in the figure. Because, beyond the range of our data, the extrapolation of (2.2) agrees well with these two theoretical results, we believe that extrapolating (2.2) to hurricane-strength winds is consistent with theory. The Charnock relation from previous versions of our algorithm (Andreas et al. 2008; cf. Fairall et al. 1996, 2003; see Figure 2) predicts progressively increasing drag for U_{N10} above 30 m s^{-1} that is not compatible with the needs of hurricane models.

The crucial feature of (2.2) that makes extrapolating it meaningful is that in higher winds it reduces to

$$u_* = 0.0583 U_{N10} - 0.243, \quad (2.3)$$

where u_* and U_{N10} are still in m s^{-1}. As such, for higher winds, our hyperbola easily gives the more familiar 10-m, neutral-stability drag coefficient:

$$C_{DN10} \equiv \left(\frac{u_*}{U_{N10}} \right)^2 = 3.40 \times 10^{-3} \left(1 - \frac{4.17}{U_{N10}} \right)^2. \quad (2.4)$$

That is, (2.2) predicts C_{DN10} to increase monotonically with increasing wind speed but to roll off to an asymptotic value of 3.40×10^{-3} at very high wind speeds.

As (2.2) and (2.4) do, limiting the value of the drag coefficient in high winds to values much less than those predicted by the Charnock relation, for example, seems to have helped recent hurricane models (e.g., Jarosz et al. 2007; Sanford et al. 2007; Chiang et al. 2011). In addition, for major hurricane wind speeds of 60–75 m s^{-1}, (2.4) gives C_{DN10} values near 3.0×10^{-3}. Coincidentally, this is the limiting value that Tang and Emanuel (2012) imposed in their recent hurricane modeling study.

For completeness, we mention how we calculate U_{N10} in our analysis or in implementing our algorithm. We use (Andreas et al. 2012)

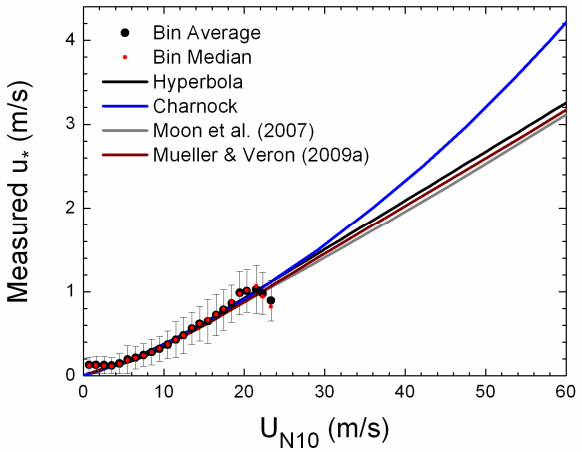

FIG. 2. Summary of the drag analysis in Andreas et al. (2012). The black circles are averages in U_{N10} bins 1 m s^{-1} wide. The error bars are ±2 standard deviations in the bin populations. The red circles are medians in these same bins. The curves denote the hyperbola (2.2), which is the drag relation in our flux algorithm, and the theoretical results of Moon et al. (2007) and Mueller and Veron (2009a). The blue curve is the Charnock relation from our previous algorithm (Andreas et al. 2008).

$$U_{N10} = U(z) - \frac{u_*}{k}\left[\ln(z/10) - \psi_m(z/L)\right]. \quad (2.5)$$

Here, U(z) is the measured or modeled wind speed at height z (in meters); u_* is the corresponding measured or modeled friction velocity; k (= 0.40) is the von Kármán constant; and ψ_m is the stratification correction for the wind speed profile in the atmospheric surface layer, a function of the Obukhov length, L. For ψ_m, we use the function from Paulson (1970) in unstable stratification, the function from Grachev et al. (2007) in stable stratification, and

$$\frac{z}{L} = -\frac{k z g}{\overline{T} u_*^3}\left(\frac{H_s}{\rho_a c_p} + \frac{0.61\overline{T}}{1 + 0.61\overline{Q}}\frac{H_L}{\rho_a L_v}\right). \quad (2.6)$$

In this, g is the acceleration of gravity; $\overline{T}$ and $\overline{Q}$, the average air temperature and specific humidity of the surface layer; c_p, the specific heat of air at constant pressure; and L_v, the latent heat of vaporization. Depending on whether z/L is used in our analysis or for model calculations, u_*, H_s, and H_L represent either the measured u_* and the total measured fluxes, $H_{s,T}$ and $H_{L,T}$, or the modeled u_* and the modeled interfacial fluxes, $H_{s,int}$ and $H_{L,int}$.

2.3. Interfacial Flux Algorithm

With our new expression for the surface stress—now formulated in terms of u_* and U_{N10}, (2.1a) and (2.2)—our equations for the interfacial heat fluxes differ from the common forms (cf. Garratt 1992, pp. 54ff.; Fairall et al. 1996, 2003; Perrie et al. 2005; Andreas et al. 2008) and are

$$H_{L,int} = \frac{\rho_a L_v k u_* (Q_s - Q_z)}{\ln(z/z_Q) - \psi_h(z/L)}, \quad (2.7a)$$

$$H_{s,int} = \frac{\rho_a c_p k u_* (\Theta_s - \Theta_z)}{\ln(z/z_T) - \psi_h(z/L)}. \quad (2.7b)$$

In these, Q_s and Θ_s are the specific humidity and potential temperature at the sea surface, and Q_z and Θ_z are the humidity and temperature at height z. ψ_h is the stratification correction for the scalar profiles in the atmospheric surface layer; again, we use the function from Paulson (1970) in unstable stratification and the function from Grachev et al. (2007) in stable stratification.

Finally, in (2.7), z_Q and z_T are the roughness lengths for the humidity and temperature profiles. We still use the COARE Version 2.6 expressions for these (Fairall et al. 1996). Remember, Liu et al. (1979) derived the z_Q and z_T algorithms in Version 2.6 from surface renewal theory. We do, however, limit z_Q and z_T to values greater than 7.0×10^{-8} m, approximately the mean free path of air molecules (Andreas and Emanuel 2001).

As with most bulk flux algorithms, we solve the system of equations (2.2) and (2.5)–(2.7) iteratively until u_*, $H_{s,int}$, and $H_{L,int}$ converge. This iteration usually takes about three steps.

Notice in (2.1a), (2.2), (2.5), and (2.7) the conspicuous absence of the aerodynamic roughness length z_0. Because our new drag relation is formulated without z_0, it avoids all of the uncertainties in formulations of z_0, including the severe self-correlation in attempts to evaluate its behavior from data (e.g., Mahrt et al. 2003).

2.4. Full Spray-Mediated Flux Model

Microphysical modeling demonstrates that, under constant environmental conditions, the temperature T and radius r of a sea spray droplet evolve as functions of the time since formation t approximately as (Andreas 1990, 2005; Andreas and DeCosmo 1999, 2002)

$$\frac{T(t) - T_{eq}}{\Theta_s - T_{eq}} = \exp(-t/\tau_T), \qquad (2.8)$$

$$\frac{r(t) - r_{eq}}{r_0 - r_{eq}} = \exp(-t/\tau_r). \qquad (2.9)$$

Here, T_{eq} is the equilibrium temperature of a saline droplet with initial radius r_0 and initial temperature Θ_s, the sea surface temperature; r_{eq} is the equilibrium radius of the same droplet; τ_T and τ_r are the e-folding times that characterize the rates of these exponential temperature and radius changes. Realize that the temperature change reflects the sensible heat transfer mediated by the droplet while the radius change implies a flux of water vapor and thus latent heat exchange.

In our data analysis, the values of T_{eq}, r_{eq}, τ_T, and τ_r in (2.8) and (2.9) come from Andreas's (1989, 1990, 1992, 1995) full microphysical model. Among other features, this model includes an equation of state for estimating the solution density of a spray droplet as it cools and evaporates. Andreas (2005), however, developed algorithms for quickly computing these microphysical quantities; we use these fast algorithms in the fast flux algorithm that we describe later.

Briefly, all four microphysical quantities in (2.8) and (2.9) depend on sea surface temperature, air temperature, relative humidity, sea surface salinity, barometric pressure, and initial droplet radius. For typical ocean salinities of 34–35 psu, τ_T is about 5 s for the largest droplets we consider, r_0 = 500 μm, and is of order 10^{-4} s for the smallest droplets, 1.6 μm. τ_r is typically three orders of magnitude longer than τ_T. That is, sensible heat exchange from spray droplets is very fast while latent heat exchange is relatively slow. See Figure 2 in Andreas and DeCosmo (2002).

To put these time scales in perspective, we also estimate the time scale for a droplet's residence in air:

$$\tau_f = \frac{H_{1/3}}{2u_f(r_0)}. \qquad (2.10)$$

In this, $u_f(r_0)$ is the terminal fall speed of droplets with initial radius r_0, and $H_{1/3}$ is the significant wave height. Because $H_{1/3}/2$ is then the significant wave amplitude, (2.10) reiterates our conceptual picture (Andreas, 1992) that the droplets most important for spray-mediated transfer are the large spume droplets (Andreas, 2002) that originate at the wave crests and fall ballistically back into the sea.

With (2.8)–(2.10), it is easy to estimate the spray-mediated sensible and latent fluxes. The spray sensible heat exchange facilitated by all droplets of radius r_0 is (Andreas 1992; Andreas et al. 2008)

$$Q_S(r_0) = \rho_w c_w (\Theta_s - T_{eq}) \bullet \left[1 - \exp(-\tau_f/\tau_T)\right]\left(\frac{4\pi r_0^3}{3}\frac{dF}{dr_0}\right). \qquad (2.11)$$

In this, ρ_w is the density of seawater, and c_w is its specific heat. From (2.8), we see that $(\Theta_s - T_{eq})\left[1 - \exp(-\tau_f/\tau_r)\right]$ is the difference between a droplet's initial temperature and its temperature when it falls back into the sea. This temperature difference is related to the sensible heat that droplets of radius r_0 transfer.

The dF/dr_0 in (2.11) is the spray generation function, which gives the number of droplets of initial radius r_0 that are produced per square meter of sea surface, per second, per micrometer increment in droplet radius (e.g., Andreas 2002). It thus has units of $m^{-2}\,s^{-1}\,\mu m^{-1}$. Hence, $(4\pi r_0^3/3)\,dF/dr_0$ is the rate at which the volume of droplets of r_0 is produced. Therefore, Q_S has units of $W\,m^{-2}\,\mu m^{-1}$ and estimates the rate of heat transfer by all droplets of radius r_0.

For dF/dr_0, we use the function from Fairall et al. (1994), as recommended in Andreas (2002). Although there has been quite a bit of recent work on the generation of film and jet droplets—see de Leeuw et al. (2011) for a review—there has been less work on the generation of spume droplets. Spume is the most important droplet class for spray-mediated transfer: see Figures 5–8 in Andreas (1992) or Figure 2 in Andreas et al. (2008). The recent papers by Mueller and Veron (2009b), Fairall et al. (2009), and Veron et al. (2012), nevertheless, do tend to corroborate the

general magnitude of the Fairall et al. (1994) function.

As with (2.11), we estimate the latent heat exchange associated with all droplets of radius r_0 as

$$Q_L(r_0) = \rho_w L_v \left\{1 - \left[\frac{r(\tau_f)}{r_0}\right]^3\right\}\left(\frac{4\pi r_0^3}{3}\frac{dF}{dr_0}\right). \quad (2.12)$$

Here, $r(\tau_f)$ comes from (2.9) with τ_f substituted for t and thus is the radius that droplets of initial radius r_0 have when they fall back into the sea. As such, $(4\pi\rho_w/3)\left\{r_0^3 - \left[r(\tau_f)\right]^3\right\}dF/dr_0$ is the mass of water that all droplets of initial radius r_0 leave in the air during their brief flights.

To get the total spray-mediated exchanges, we must integrate (2.11) and (2.12) over all droplet sizes:

$$\overline{Q}_S = \int_{1.6}^{500} Q_S(r_0)\,dr_0, \quad (2.13a)$$

$$\overline{Q}_L = \int_{1.6}^{500} Q_L(r_0)\,dr_0. \quad (2.13b)$$

These have units of a heat flux, W m^{-2}. The lower and upper limits of radius integration, 1.6 and 500 μm, are the limits of validity of the Fairall et al. (1994) spray generation function [see Andreas (2002) for the equations to compute it].

Andreas and DeCosmo (1999, 2002) termed $\overline{Q}_S$ and $\overline{Q}_L$ the *nominal* spray fluxes because they hypothesized (also Andreas et al. 2008; Andreas 2010) that the actual spray-mediated latent and sensible heat fluxes are (cf. Fairall et al. 1994; Kepert et al. 1999)

$$H_{L,sp} = \alpha\overline{Q}_L, \quad (2.14a)$$

$$H_{s,sp} = \beta\overline{Q}_S - (\alpha - \gamma)\overline{Q}_L. \quad (2.14b)$$

In these, α, β, and γ are presumed to be small, positive tuning coefficients that we evaluate from data. Although $\overline{Q}_L$ and $\overline{Q}_S$ are based on microphysics and the dF/dr_0 in them is constrained by energy arguments (e.g., Andreas 2002), there are some approximations and uncertain parameters in these theories; dF/dr_0 is one of the largest sources of this uncertainty. Nevertheless, because of their physical basis, $\overline{Q}_L$ and $\overline{Q}_S$ correctly represent the dependencies of the fluxes on environmental variables such as wind speed (i.e., Andreas 2002; Andreas et al. 2008), air and water temperatures, relative humidity, and ocean salinity (Andreas 1990, 1995, 1996, 2005; Andreas and Emanuel 2001). The α, β, and γ, therefore, minimize the impact of these uncertainties by letting us tune $H_{L,sp}$ and $H_{s,sp}$ with data, which we do shortly.

In (2.14a), α simply lets us adjust $\overline{Q}_L$ to agree with data. Similarly, in (2.14b), the β term is the direct spray-mediated sensible heat exchange. But, as Figure 1 depicts, because droplet evaporation is slower than a droplet's sensible heat exchange, all of the $\alpha\overline{Q}_L$ term in (2.14a) must be supplied by the air in the droplet evaporation layer. That is, droplet evaporation consumes sensible heat, thereby cooling the air; the $\alpha\overline{Q}_L$ term in (2.14a) must thus appear with a negative sign in (2.14b).

This cooling associated with the droplet's latent heat exchange occurs within the droplet evaporation layer, which is typically below the height z where Θ_z is specified in (2.7b). That is, (2.7b) is unaware of these near-surface temperature changes and would, thus, underestimate $H_{s,int}$. See Figure 7 in Andreas et al. (1995) or Figure 4 in Fairall et al. (1994). The $\gamma\overline{Q}_L$ term in (2.14b) is meant to recognize the steeper near-surface temperature gradient caused by spray evaporation and, thus, adds an extra sensible heat flux to augment the flux missed in (2.7b).

3. DATA

The data that we use in our analysis are some of the same sets that Mahrt et al. (2012), Andreas et al. (2012, 2013), and Vickers et al. (2013) have been using recently. Table 1 lists these datasets. The key feature of all these data is that u_*, $H_{L,T}$, and $H_{s,T}$ were measured with eddy-covariance instruments. Andreas et al. (2013) review the instruments used for these measurements.

Only the HEXOS and FASTEX sets include measurements of significant wave height that we need in (2.10). For all the other datasets, we estimated $H_{1/3}$ from Andreas and Wang's (2007) algorithm.

Table 1. The datasets used in this study. The "Number of Observations" is the number of cases left after the screening described in the text. The "Reference" provides additional details on a dataset.

Dataset	Number of Observations	Platform/Location	Reference
CARMA4[a]	437	CIRPAS Twin Otter, off coast of southern California	Vickers et al. (2013)
CBLAST-weak[b]	2	Long-EZ aircraft, Martha's Vineyard, Massachusetts	Edson et al. (2007)
FASTEX[c]	263	*R/V Knorr*, transect across the North Atlantic	Persson et al. (2005)
GFDex[d]	102	FAAM BAE 146 aircraft, Irminger Sea and Denmark Strait	Petersen and Renfrew (2009)
GOTEX[e]	817	NCAR C-130, Gulf of Tehuantepec	Romero and Melville (2010)
HEXOS[f]	173	Meetpost Noordwijk platform, North Sea	DeCosmo (1991), DeCosmo et al. (1996)
MABLEB[g]	40	CIRPAS Twin Otter, off Monterey, California	Vickers et al. (2013)
Monterey	556	CIRPAS Twin Otter, off Monterey, California	Mahrt and Khelif (2010)
POST[h]	171	CIRPAS Twin Otter, off Monterey, California	Vickers et al. (2013)
RED[i]	351	CIRPAS Twin Otter, east of Oahu, Hawaii	Anderson et al. (2004)
SHOWEX[j] Nov '97	366	Long-EZ aircraft, off coast of Virginia and North Carolina	Sun et al. (2001)
TOGA COARE[k]	742	NCAR Electra, western equatorial Pacific Ocean	Sun et al. (1996), Vickers and Esbensen (1998)

[a]Cloud-Aerosol Research in the Marine Atmosphere, experiment 4.
[b]Coupled Boundary Layers and Air-Sea Transfer in weak winds.
[c]Fronts and Atlantic Storm-Tracks Experiment.
[d]Greenland Flow Distortion experiment.
[e]Gulf of Tehuantepec Experiment.
[f]Humidity Exchange over the Sea experiment.
[g]Marine Atmospheric Boundary Layer Energy Budget experiment.
[h]Physics of the Stratocumulus Top experiment.
[i]Rough Evaporation Duct experiment.
[j]Shoaling Waves Experiment.
[k]Tropical Ocean-Global Atmosphere Coupled Ocean-Atmosphere Response Experiment.

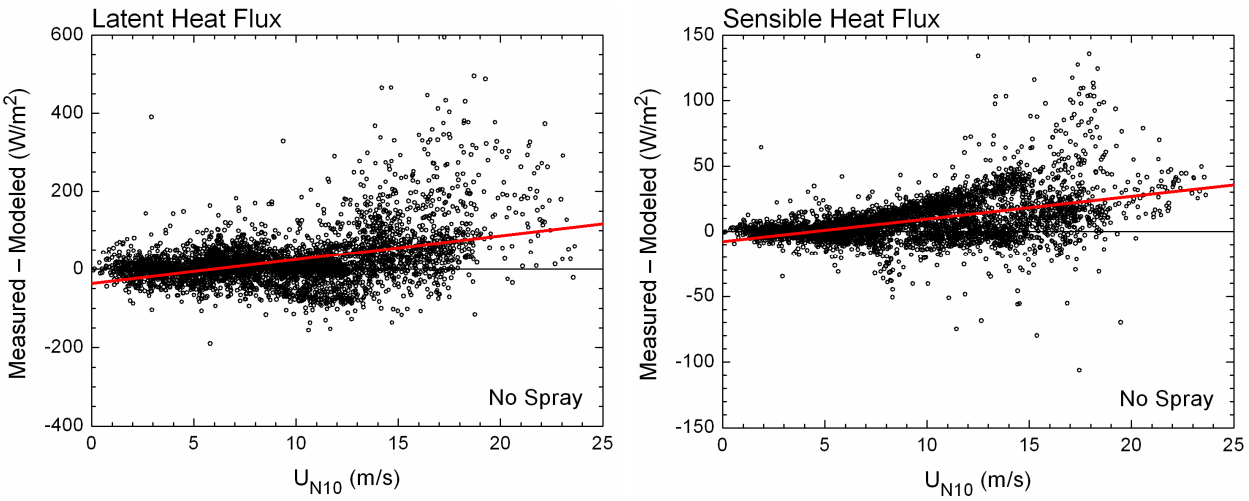

FIG. 3. Eddy-covariance measurements of the latent (left panel) and sensible (right panel) heat fluxes are compared with values modeled with only the interfacial part (i.e., $H_{L,int}$, $H_{s,int}$) of our flux algorithm. The independent variable is the 10-m, neutral-stability wind speed, U_{N10}, (2.5). The red lines are the least-squares fits through all the data. For $U_{N10} \geq 10$ m s^{-1}, in the latent heat flux panel, the bias is 43.4 W m^{-2} and the correlation coefficient is 0.496; in the sensible heat flux panel, 16.4 W m^{-2} and 0.254, respectively. On the basis of all four values, we thus reject the null hypothesis with better than 95% confidence.

We had other datasets available besides those listed in Table 1, and the datasets in Table 1 usually contained more observations than shown in the table. We screened all the data, however, to focus on conditions pertinent to our analysis. First, a data run needed to include reliable measurements of u_*, $H_{L,T}$, $H_{s,T}$, wind speed, sea surface temperature, air temperature, and humidity. For example, we eliminated about 40 GOTEX runs because the ogives (e.g., Oncley et al. 1996) for the sensible heat flux did not converge.

Most of the cases in the CBLAST set had relative humidities that were high, often above 100%. Not only do these values seem unreliable; but, when we used them, our calculations of $\overline{Q}_L$ and $\overline{Q}_S$ did not converge. Hence, we eliminated almost all of the CBLAST data. The relative humidity in a few other datasets was occasionally too high to yield good calculations of $\overline{Q}_L$ and $\overline{Q}_S$, and we eliminated these runs, too. The effect is that our flux algorithm is not as well tested in high relative humidities, where spray droplets grow from condensation, as it is for lower relative humidities.

All the aircraft data listed in Table 1 were collected at fight levels of 50 m or less and, thus, generally represent surface conditions. In stable stratification, however, because of flux divergence, the flight-level fluxes may differ significantly from the surface fluxes. As in Andreas et al. (2012, 2013), we therefore calculated z_{ac}/L for each aircraft run, where z_{ac} is the aircraft's flight level and L is the measured Obukhov length. We retained for our analysis only data for which $-\infty < z_{ac}/L \leq 0.1$. That is, from the aircraft sets, our analysis used data collected only in weakly stable stratification or in unstable stratification.

On the other hand, the FASTEX and HEXOS measurements were made at heights below 20 m. Any flux divergence in these sets would be less than the experimental uncertainty; we therefore retained all these data, regardless of stratification.

4. QUANTIFYING THE SPRAY AND INTERFACIAL FLUXES

Our hypothesis is that spray-mediated transfer is a significant route for the scalar air-sea fluxes. Hence, we should first evaluate the null hypothesis—that it is not. Figure 3 shows this test of the null hypothesis.

Figure 3 compares the measured heat fluxes in our dataset (i.e., $H_{L,T}$ and $H_{s,T}$) with fluxes modeled with (2.1), (2.2), and (2.5)–(2.7). In other

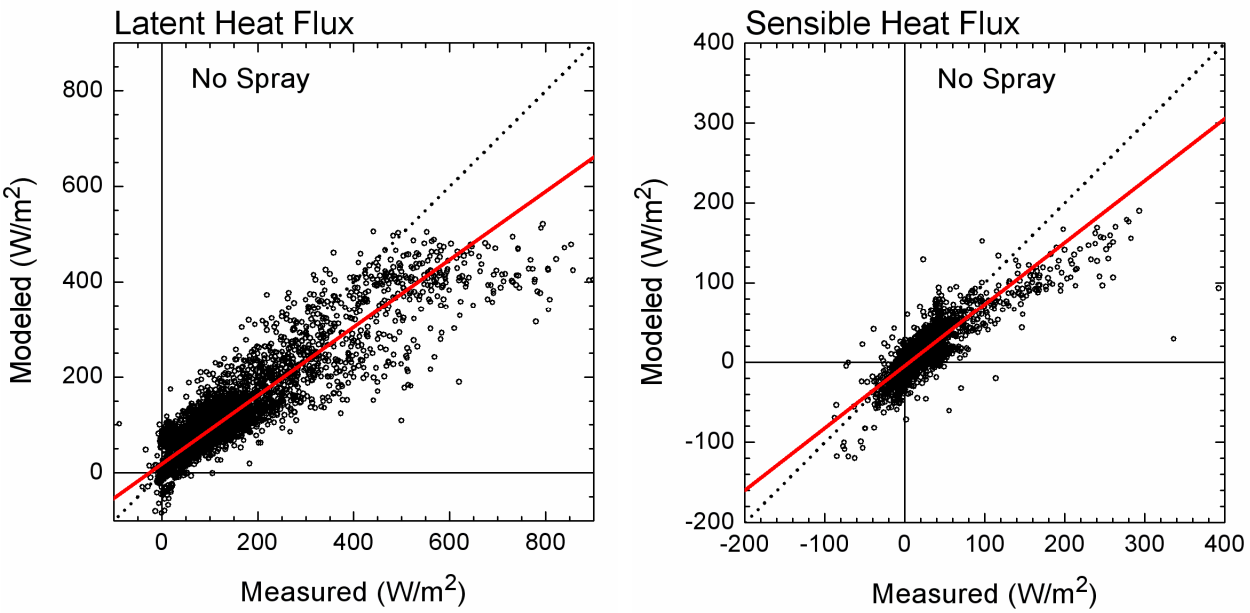

FIG. 4. The same flux data as in Figure 3 are here presented as scatter plots. That is, the modeled fluxes have no spray contribution. In each panel, the dashed black line is 1:1, and the red line is the best fit through the data calculated as the bisector of y-versus-x and x-versus-y least-squares lines. The correlation coefficient is 0.910 in the latent heat flux panel and 0.834 in the sensible heat flux panel.

words, we first ignored any modeled spray contributions by setting $\alpha = \beta = \gamma = 0$ in (2.14). Figure 3 plots as the dependent variable the measured minus the modeled flux. This quantity lets us evaluate the bias in our model and how this bias depends on wind speed. If the null hypothesis were true, the bias would be near zero at all wind speeds.

In both panels in Figure 3, the bias is near zero for wind speeds up to 10 m s^{-1}, the range over which the crucial z_Q and z_T parameterizations in the COARE Version 2.6 algorithm have been well validated (Fairall et al. 1996; Grant and Hignett 1998; Chang and Grossman 1999; Brunke et al. 2002). That is, we again confirm that the interfacial flux algorithm we use is accurate for wind speeds where we expect no spray contributions.

At higher wind speeds, however, both measured heat fluxes increasingly exceed the modeled fluxes with increasing wind speed. This behavior is the signature of spray-mediated transfer because dF/dr_0 in (2.11) and (2.12) goes, roughly, as the third power of wind speed while $H_{L,int}$ and $H_{s,int}$ in (2.7) are almost linear in wind speed.

The red lines in Figure 3 are least-squares fits through the data and have slopes significantly above zero: The bias has a positive wind speed dependence. Likewise, correlation coefficients for Measured–Modeled versus U_{N10} in both panels are non-zero with better than 95% confidence: The bias is correlated with wind speed. See Andreas et al. (2008) to learn how we calculate the confidence intervals for these fitting metrics. In the cases of Figure 3, these least-squares lines are more suggestive than quantitative because both panels in Figure 3 have two regimes: the $0 \le U_{N10} \le 10$ m s^{-1} regime, where the data are horizontal and collect around y = 0; and the regime above 10 m s^{-1}, where the data have a positive slope.

Figure 4 shows another rendering of the flux data in Figure 3. These are scatter plots of the modeled versus the measured latent and sensible heat fluxes—again, with no spray contribution in the modeled fluxes. Figure 4 reiterates what we saw in Figure 3: A state-of-the-art interfacial flux algorithm cannot explain our measurements, especially when the measured fluxes are large.

As counterpoint to Figure 3, Figure 5 shows measurements now compared with modeled values that also include spray-mediated transfer, as computed from (2.1) and (2.9)–(2.14). With the relatively small, constant tuning coefficients of

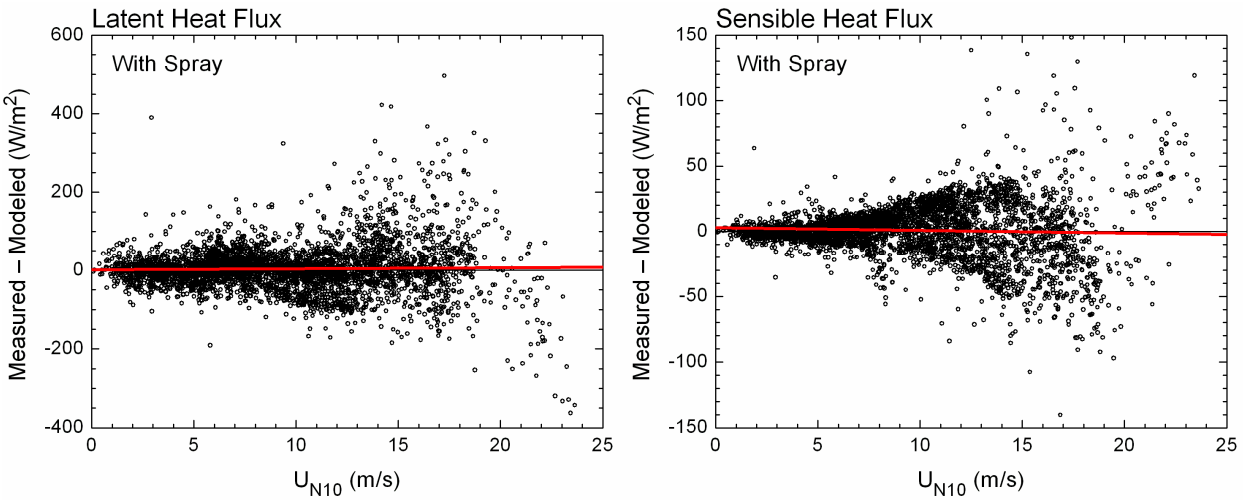

FIG. 5. As in Figure 3, but here the modeled fluxes now also include the spray-mediated fluxes in (2.1), where $\alpha = 2.46$, $\beta = 15.15$, and $\gamma = 1.77$ in (2.14). For $U_{N10} \geq 10$ m s^{-1}, the bias in the latent heat panel is 3.70 W m^{-2} and the correlation coefficient is 0.0225; in the sensible heat flux panel, 0.095 W m^{-2} and −0.102. All four of these values are indistinguishable from zero at the 95% confidence level.

$\alpha = 2.46$, $\beta = 15.15$, and $\gamma = 1.77$, we explain both the magnitude and the wind speed dependence of the measurements. That is, the red fitting lines in Figure 5 are essentially both horizontal and near $y = 0$. The caption for Figure 5 gives the fitting metrics in the crucial region where $U_{N10} \geq 10$ m s^{-1}: The bias in this region in both plots is statistically indistinguishable from zero, as is the correlation coefficient.

In effect, the theoretically based analyses represented in Figures 3 and 5 have separated the measured fluxes into interfacial and spray contributions. Clearly, data analysis alone cannot accomplish this separation because of how differently the interfacial and spray fluxes scale (cf. Andreas 2011).

On comparing the respective panels in Figures 3 and 5, we see that, between U_{N10} of 15 and 25 m s^{-1}, the spray latent heat flux increases, on average, from about 100 to 200 W m^{-2}. Meanwhile, the spray sensible heat flux increases from about 20 to 50 W m^{-2}. Moreover, both spray fluxes become significant in the U_{N10} region 10–12 m s^{-1}. By "significant," we mean that, starting in this wind speed range, the spray flux typically has a magnitude that is at least 10% of the magnitude of its respective interfacial flux (cf. Andreas and DeCosmo 2002; Andreas et al. 2008; Andreas 2010).

Figure 6 is the companion to Figure 4; it again shows scatter plots of the latent and sensible heat fluxes, but now the modeled fluxes include the spray contributions modeled as above. Comparing Figures 4 and 6 again demonstrates how accounting for spray has improved our representation of the measured fluxes. Although the correlation coefficients given in the caption to Figure 6 are only marginally better than for the "No Spray" comparisons in Figure 4, the "With Spray" results are distinctly better. In particular, for the latent heat flux, the bias (measured minus modeled) in the "No Spray" panel in Figure 4 is 21.3 W m^{-2} but in the "With Spray" panel in Figure 6 is only 3.3 W m^{-2}. Likewise, for the sensible heat flux, the bias in the "No Spray" panel is 8.6 W m^{-2} but in the "With Spray" panel is only 1.0 W m^{-2}.

We are disappointed, nevertheless, that $\beta = 15.15$ turned out to be large. But it was also fairly large in our two previous analyses with much smaller datasets that had wind speeds limited to about 20 m s^{-1}; Andreas and DeCosmo (2002) evaluated it to be 6.5, and Andreas *et al.* (2008) obtained 10.5. A hypothesis to explain the size of β and its progression in values is that more or larger spume droplets are produced than assumed in the dF/dr_0 function from Fairall et al. (1994); and, as with all spray, the production of these droplets increases with wind speed.

More large spume droplets would translate to larger measured sensible heat fluxes than we would model with our current dF/dr_0; β would

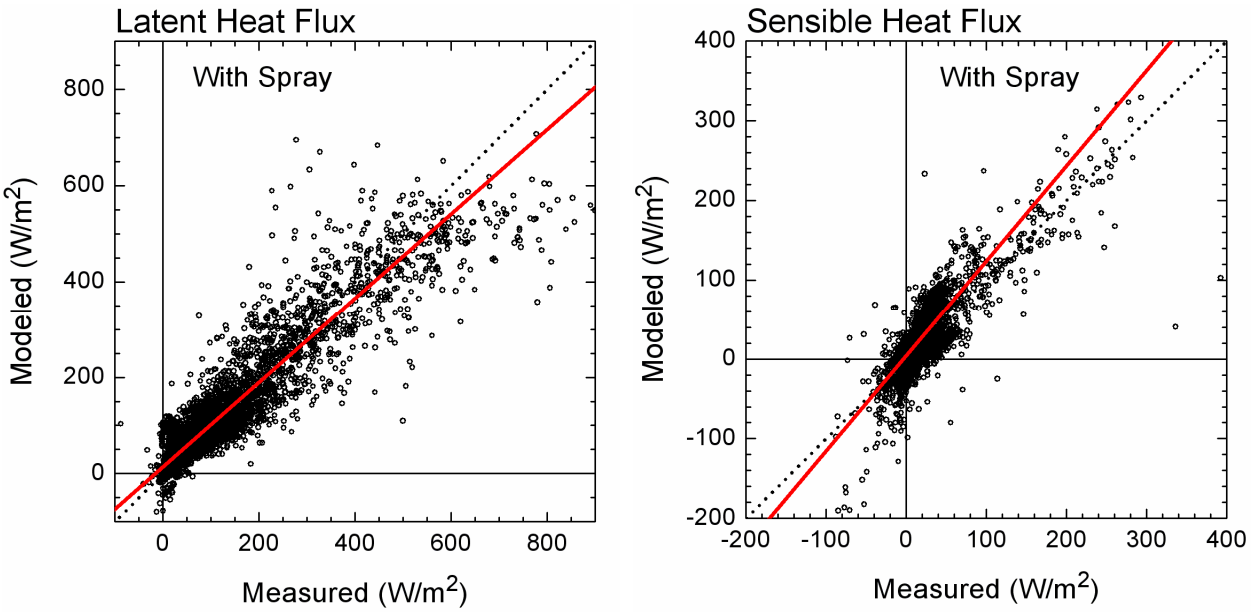

FIG. 6. Scatter plots as in Figure 4 but here with the flux data from Figure 5, which include modeled spray contributions. The correlation coefficient in the latent heat flux panel is 0.917; in the sensible heat flux panel, 0.845.

therefore need to be bigger than the expected value of one to account for the excess spray-mediated flux. On the other hand, these large droplets would minimally affect the spray latent heat flux because they would fall back into the sea before releasing appreciable water vapor. Consequently, $\alpha = 2.46$ is still of order one.

Although far from conclusive for ocean conditions, three laboratory studies hint at the existence of these large and more plentiful spume droplets. In wind-wave tunnels, Anguelova et al. (1999), Fairall et al. (2009), and Veron et al. (2012) all observed significant numbers of spume droplets with radii larger than 500 µm, the upper limit in the Fairall et al. (1994) spray generation function. In the Fairall et al. (2009) and Veron *et al.* (2012) studies, production rates were also higher for droplet radii above 200 µm than predicted by our current dF/dr_0.

The existence of these unanticipated large droplets could also, at least in part, explain the more widely scattered points above 10 m s^{-1} in the sensible heat flux panels than in the latent heat flux panels in Figures 3 and 5. The small measured sensible heat fluxes depicted in Figures 4 and 6 and the consequent poorer signal-to-noise ratio in these data also contribute to the scatter in the plots of sensible heat flux.

5. FAST SPRAY-FLUX ALGORITHM

The calculations that we made to obtain the spray-mediated fluxes in Figures 5 and 6 (described in Section 3) are too intensive for large-scale computer models. We have therefore developed a fast spray-flux algorithm to complement the fast interfacial-flux algorithm represented in (2.1a), (2.2), and (2.5)–(2.7).

When Andreas et al. (2008, their Figure 2) plotted $Q_L(r_0)$ and $Q_S(r_0)$ versus r_0 [see also Figures 5–8 in Andreas (1992) and Figure 16 in Andreas et al. (1995)], they observed that Q_L had a large peak in the vicinity of $r_0 = 50$ µm and that Q_S had a similarly large peak near $r_0 = 100$ µm. They thus hypothesized that the microphysical behavior of 50 µm droplets might be a good indicator of $H_{L,sp}$ and that the behavior of 100 µm droplets might be a good indicator of $H_{s,sp}$. They termed these droplets *bellwethers* for the fluxes (also Andreas and Emanuel 2001).

Under this hypothesis, Andreas et al. (2008) wrote

$$H_{L,sp} = \alpha \overline{Q}_L = \rho_w L_v \left\{ 1 - \left[\frac{r(\tau_{f,50})}{50\,\mu\text{m}} \right]^3 \right\} V_L(u_{*,B}) \qquad (5.1)$$

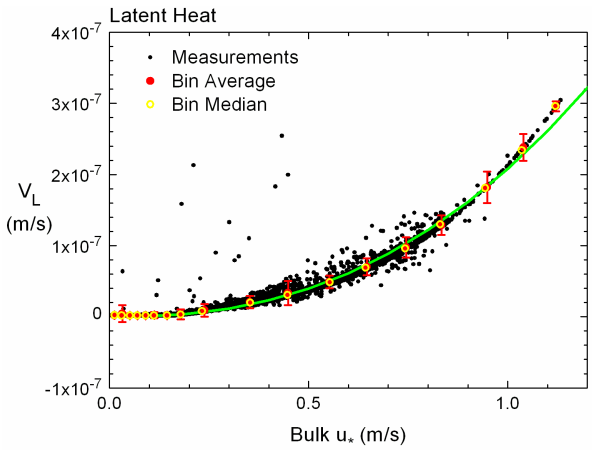

FIG. 7. The values of $\alpha\overline{Q}_L$ deduced from the analysis that produced the latent heat flux panel in Figure 5 are here used to evaluate the wind function V_L from (5.3). The horizontal axis is the bulk friction velocity ($u_{*,B}$) deduced from solving the interfacial flux algorithm. The plot also shows bin averages and bin medians in $u_{*,B}$ bins. The error bars on the bin averages are ±1 standard deviation in the bin population. The green curve is the best fit through the data in the nonlinear region and is (5.5).

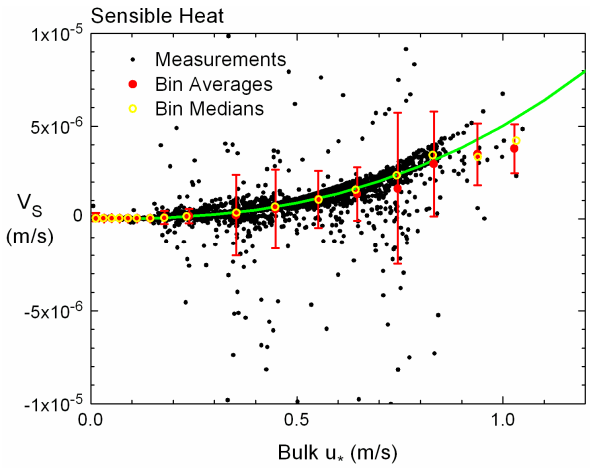

FIG. 8. As in Figure 7, except here the values of $\beta\overline{Q}_S - (\alpha-\gamma)\overline{Q}_L$ deduced from the analysis that produced the sensible heat flux panel in Figure 5 are used to evaluate the wind function V_S from (5.4). The green curve is (5.6).

and

$$\begin{aligned} H_{s,sp} &= \beta\overline{Q}_S - (\alpha-\gamma)\overline{Q}_L \\ &= \rho_w c_w (\Theta_s - T_{eq,100}) V_s(u_{*,B}) \end{aligned}. \qquad (5.2)$$

In (5.1), $\tau_{f,50}$ is the residence time of droplets with 50 μm initial radius; the 50 μm is, of course, that initial radius [compare (2.12)]. In (5.2), $T_{eq,100}$ is the equilibrium temperature of droplets with 100 μm initial radius [compare (2.11)]. Because 100 μm droplets almost always reach temperature equilibrium before they fall back into the sea, we need not include in (5.2) a dependence on residence time.

The V_L and V_S in (5.1) and (5.2) are *wind functions* that, we hypothesize, depend on the bulk friction velocity, $u_{*,B}$, obtained by iteratively solving (2.2) and (2.5)–(2.7). Because we determined $\alpha\overline{Q}_L$ and $\beta\overline{Q}_S - (\alpha-\gamma)\overline{Q}_L$ in the last section, we can evaluate V_L and V_S from these data:

$$V_L(u_{*,B}) = \frac{\alpha\overline{Q}_L}{\rho_w L_v \left\{1 - \left[\frac{r(\tau_{f,50})}{50\,\mu m}\right]^2\right\}}, \qquad (5.3)$$

$$V_S(u_{*,B}) = \frac{\beta\overline{Q}_S - (\alpha-\gamma)\overline{Q}_L}{\rho_w c_w (\Theta_s - T_{eq,100})}. \qquad (5.4)$$

Figures 7 and 8 show our evaluations of these functions.

A crucial issue in evaluating (5.3) and (5.4) and in plotting Figures 7 and 8 is to realize how (5.1) and (5.2) are to be used. These are fast algorithms for use in air-sea interaction models and similar computations. These applications will not have the luxury of the full microphysical model that yielded $\overline{Q}_L$ and $\overline{Q}_S$ and the related calculations of T_{eq}, r_{eq}, τ_T, and τ_r [see (2.11) and (2.12)]. Instead, in evaluating (5.3) and (5.4), we used Andreas's (2005) fast microphysical algorithms to compute $r_{eq,50}$, $\tau_{r,50}$, and $T_{eq,100}$, where $r_{eq,50}$ and $\tau_{r,50}$ are the equilibrium radius and e-folding time for droplets with r_0 = 50 μm that are needed to evaluate $r(\tau_{f,50})$. After all, this is how a bulk flux algorithm would obtain $r_{eq,50}$, $\tau_{r,50}$, and $T_{eq,100}$ for computing (5.1) and (5.2).

Furthermore, the independent variable in Figures 7 and 8 is the bulk friction velocity, not the measured friction velocity. Again, a bulk flux

algorithm can produce only $u_{*,B}$.

The averages and the medians in Figures 7 and 8 agree well. Hence, the samples within each bin are well behaved. We removed fewer than 10 extreme outliers each from the V_S and V_L datasets.

Both Figures 7 and 8 show two regimes: a region for $u_{*,B} < 0.15 m s^{-1}$, nominally, where V_L and V_S are practically zero, and the region above $u_{*,B} = 0.15 m s^{-1}$, where V_L and V_S increase faster than linearly with $u_{*,B}$. The green curves in the figures are our fits to the data and are

$$V_L = 1.76 \times 10^{-9} \quad \text{for } 0 \le u_{*,B} \le 0.1358 m s^{-1}, \quad (5.5a)$$

$$V_L = 2.08 \times 10^{-7} u_{*,B}^{2.39} \quad \text{for } 0.1358 m s^{-1} \le u_{*,B}, \quad (5.5b)$$

and

$$V_S = 3.92 \times 10^{-8} \quad \text{for } 0 \le u_{*,B} \le 0.1480 m s^{-1}, \quad (5.6a)$$

$$V_S = 5.02 \times 10^{-6} u_{*,B}^{2.54} \quad \text{for } 0.1480 m s^{-1} \le u_{*,B}. \quad (5.6b)$$

In these, V_L, V_S, and $u_{*,B}$ are all in m s^{-1}. Friction velocities of 0.1358 to 0.1480 m s^{-1} correspond to 10-m wind speeds of 4.5–5 m s^{-1}, which is the range where whitecap coverage reaches about 0.1% (e.g., de Leeuw et al. 2011).

Our bulk flux algorithm for the spray-mediated fluxes now comprises (2.9), (2.10), (5.1), (5.2), (5.5), (5.6), and the fast microphysical algorithms in Andreas (2005). Because of the high-order dependence on $u_{*,B}$ in (5.5) and (5.6), the spray fluxes become increasingly important with increasing wind speed. Remember, the interfacial fluxes, (2.7), depend linearly on $u_{*,B}$ for all wind speeds.

6. DISCUSSION

6.1. Spray and Interfacial Coupling

In our analysis and in our resulting bulk flux algorithm, there is no explicit coupling between the interfacial processes and the spray processes. In both the analysis and the algorithm, we first use the interfacial components of our algorithm to iteratively compute $u_{*,B}$, $H_{L,int}$, $H_{s,int}$, and L. The relevant equations are (2.1a), (2.2), and (2.5)–(2.7).

In the spray analysis, we then used the full microphysical model, described in Section 2.4, to compute $\overline{Q}_L$ and $\overline{Q}_S$. For these calculations, we used $u_{*,B}$, $H_{L,int}$, $H_{s,int}$, and L to compute the 10-meter values of wind speed, air temperature, and relative humidity because these are reference conditions that we used for computing $H_{1/3}$, dF/dr_0, T_{eq}, and r_{eq}, for instance.

In the bulk flux algorithm for the spray fluxes, we again use the 10-meter reference values and only $u_{*,B}$ from the interfacial algorithm to compute $H_{L,sp}$ and $H_{s,sp}$ in one step. In other words, we do not add $H_{L,sp}$ and $H_{s,sp}$ to $H_{L,int}$ and $H_{s,int}$, respectively; recalculate L; and then iterate on all fluxes again. While this iteration would be straightforward, it would introduce complexity that seems unjustified in light of the several uncertainties in our understanding of spray processes.

Moreover, because the spray-mediated fluxes increase as high powers of $u_{*,B}$, cases of large spray heat fluxes correspond with stratification that is tending to neutral because L is proportional to $u_{*,B}^3$ [see (2.6)]. In other words, assuming that the spray heat fluxes do not affect atmospheric stratification is a reasonable first-order approximation.

The literature, nevertheless, contains a host of other opinions as to whether there is coupling between the interfacial and spray processes. Most such speculation is based on the premise that enough spray is present in the near-surface air to increase its density (e.g., Lighthill 1999; Lykossov 2001; Bao et al. 2011; Kudryavtsev and Makin 2011) and, thus, to push the Obukhov length toward stable stratification. In some analyses, this spray mass loading is so extreme that the resulting stable stratification decouples the lower, spray-laden atmosphere from the surface and thereby reduces the surface stress (e.g., Barenblatt et al. 2005; Kudryavtsev 2006). Under any of these scenarios, because interfacial and spray processes both influence the Obukhov length, both sets of equation are coupled and must be solved simultaneously.

We have, however, not found the arguments for spray to affect atmospheric stratification very compelling. The analyses that do suggest dynamically important spray effects on stratification usually assume spray mass loadings that are unrealistically large (e.g., Pielke and Lee 1991; Barenblatt et al. 2005) or spray generation rates that go as very high powers of wind speed

[as u_*^5 in Kudryavtsev (2006), for instance] and, therefore, do not appear energetically consistent.

Furthermore, two recent modeling studies found negligible influence from spray on near-surface stratification. In a study that explicitly treated tropical cyclones and high winds, where spray is plentiful, Shpund et al. (2011) considered the effects of large eddies, which are common in convective conditions. In their model, these eddies dispersed the spray upward; it therefore did not collect near the surface where it might affect the density stratification (also Shpund et al. 2012).

In a direct numerical simulation of turbulent Couette flow that included the tracking of millions of spray-like Lagrangian particles, Richter and Sullivan (2013) studied the effects of the particles on near-surface momentum transfer. While they found that the particles could carry a significant fraction of the near-surface stress, they also found that the total stress on the surface was largely independent of the particle concentration. Richter and Sullivan then explained that theirs is basically the same conclusion that Andreas (2004) reached: Spray droplets can alter the turbulent stress profile—though not the total stress—through particle inertia but not by enhancing the density stratification.

Hence, we reiterate our decision not to couple the spray and interfacial processes. We find no compelling evidence that the increased complexity necessary in our analysis and algorithm would be beneficial and see no obvious path to how to do this coupling.

6.2. Examples of Sensitivity

Andreas et al. (2008) and Andreas (2010) (see also Perrie et al. 2005) presented sensitivity plots to show, respectively, how the parameterized scalar fluxes in Versions 3.2 and 3.4 of our flux algorithm depended on state variables like 10-m wind speed, sea surface temperature, and relative humidity at 10 m. For comparison, we present similar sensitivity plots in Figures 9, 10, and 11. In these, Θ_s is the surface temperature, as in (2.7b); T_{10}, though, is the actual air temperature at 10 m rather than the potential temperature Θ.

Figure 9, which shows how the interfacial and spray sensible and latent heat fluxes depend on the 10-m wind speed, U_{10}, reiterates observations that we have already made. Both interfacial fluxes ($H_{L,int}$ and $H_{s,int}$) are close to linear in wind speed, while both spray fluxes ($H_{L,sp}$ and $H_{s,sp}$) increase at

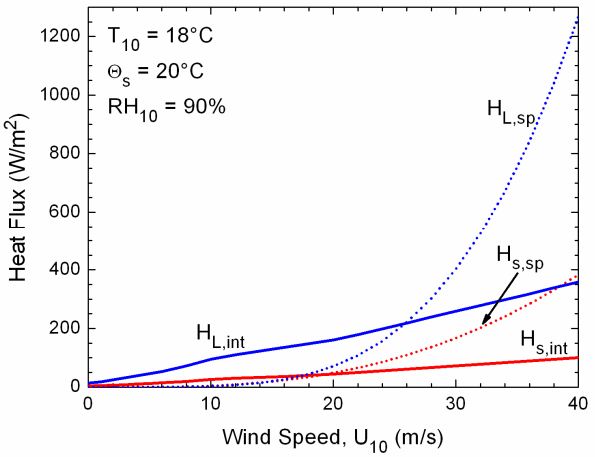

FIG. 9. Calculations of the interfacial and spray latent and sensible heat fluxes from our new bulk flux algorithm for a range of 10-m wind speed, U_{10}. The sea surface temperature (Θ_s) and 10-m values of air temperature (T_{10}) and relative humidity (RH_{10}) are fixed at the values indicated. The sea surface salinity is 34 psu, and the barometric pressure is 1000 mb.

rates that are faster than linear in wind speed. As a result, though both spray fluxes are small for $U_{10} < 10$ m s^{-1}, both overtake their respective interfacial fluxes as the wind speed increases. For the conditions depicted, the spray sensible heat flux passes the interfacial sensible heat flux for U_{10} of about 19 m s^{-1}; the spray latent heat flux passes the interfacial latent heat flux at about 26 m s^{-1}.

In Figure 10, which shows how the fluxes depend on surface temperature, both sensible heat fluxes change little because the sea–air temperature difference is fixed at 2°C. The interfacial sensible heat flux decreases just a few watts per square meter with increasing surface temperature. Meanwhile, the spray sensible heat flux increases by about 12 W m^{-2} over the temperature range depicted because, with increasing air temperature, $\Theta_s - T_{eq,100}$ [see (5.2)] increases slowly (Andreas 1995).

On the other hand, both interfacial and spray latent heat fluxes increase by 100–200% over the surface temperature range shown in Figure 10. For the interfacial flux, this increase is in response to $Q_s - Q_z$ in (2.7a), which is an exponentially increasing function of temperature. The spray latent heat flux increases so much with increasing temperature because the evaporation rate of spray

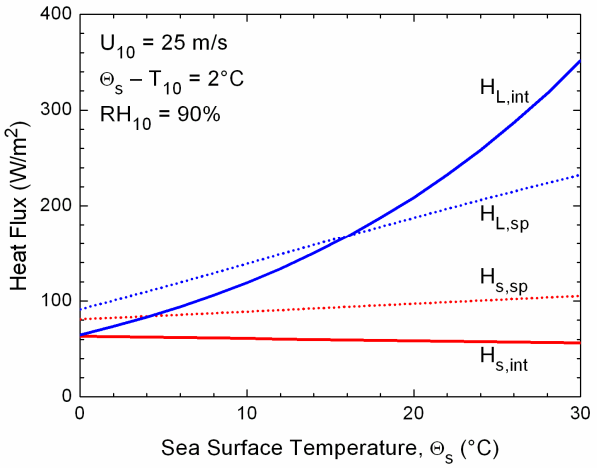

FIG. 10. As in Figure 9, but here sea surface temperature (Θ_s) varies while 10-m wind speed (U_{10}) and relative humidity (RH_{10}) are held fixed. At each surface temperature, the 10-m air temperature (T_{10}) is 2°C less than Θ_s.

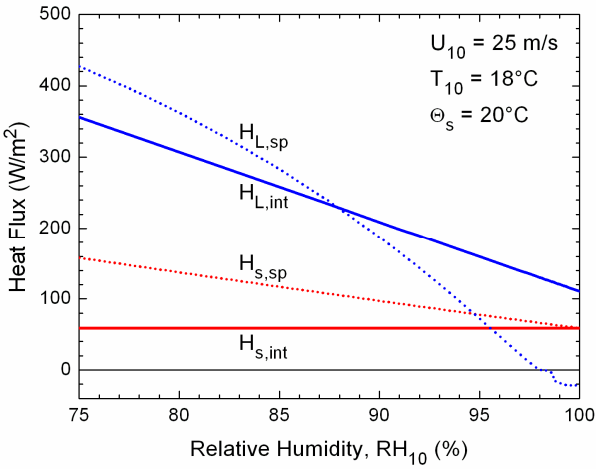

FIG. 11. As in Figures 9 and 10, but here the 10-m relative humidity (RH_{10}) varies while wind speed (U_{10}), air temperature (T_{10}), and surface temperature (Θ_s) are held fixed.

droplets increases exponentially with temperature. In effect, $r(\tau_{f,50})$ in (5.1) gets closer and closer to the equilibrium radius with increasing temperature because the time scale for radius evolution, τ_r, gets shorter and shorter (Andreas 1990). This strong temperature dependence in the spray latent heat flux and the magnitude of the flux at high temperatures again imply that modeling this flux correctly could be crucial for predicting hurricane intensity.

The last sensitivity plot, Figure 11, considers how the fluxes depend on the 10-m relative humidity. The figure represents relative humidities above 75% because 75% is the nominal deliquescence point of saltwater droplets (e.g., Pruppacher and Klett 2010, pp. 112f.). Our microphysical model does not currently treat lower relative humidities and the solid or quasi-liquid particles associated with them.

The interfacial sensible heat flux is largely independent of relative humidity at U_{10} = 25 m s^{-1}. The interfacial latent heat flux decreases with increasing relative humidity because, for this figure, Q_s in (2.7a) is fixed while Q_z increases with increasing relative humidity but is always smaller than Q_s.

The spray fluxes both decrease with increasing relative humidity. The spray sensible heat flux decreases because $T_{eq,100}$ in (5.2) rises toward the air temperature with increasing relative humidity (Andreas 1995) and can, in fact, exceed the air temperature (though not Θ_s in Figure 11) for relative humidities above 98.1% (for a surface salinity of 34 psu). The spray latent heat flux decreases because the equilibrium radius [$r_{eq,50}$ in (2.9)] of droplets initially at 50 μm radius increases toward 50 μm with increasing humidity. The ratio $r(\tau_{f,50})/50\,\mu m$ in (5.1) thus approaches 1. At relative humidities above about 98.1%, the droplets grow rather than evaporate; and $H_{L,sp}$ changes sign.

One conclusion that we intend to demonstrate with Figures 9–11 is that the spray and interfacial fluxes do not scale the same. Consequently, parameterizing the total fluxes from data analysis alone—using interfacial scaling, for example—is not possible. See Andreas (2011) for demonstrations of how poor the results can be with this approach. Our approach, in contrast, has been to formulate physics-based models for both flux routes and to test these models against the measured total fluxes.

7. SUMMARY

For winds above 10–12 m s^{-1}, the spray route for the air-sea transfers of heat, moisture, and enthalpy becomes a significant fraction (i.e., at least 10%) of the interfacial route. We have here thus developed a fast bulk flux algorithm that explicitly treats both the interfacial and spray routes for these scalar fluxes. We identify this

algorithm as Version 4.0.

A cornerstone of this new algorithm is a new drag relations that predicts $u_{*,B}$, the bulk friction velocity, from U_{N10} for all wind speeds, where $\tau = \rho_a u_{*,B}^2$ is the surface stress or surface momentum flux. Because this new relation naturally predicts $u_{*,B} > 0$ for $U_{N10} = 0$, we need not include the rather arbitrary gustiness parameterization (e.g., Fairall et al. 1996, 2003; Bourassa et al. 1999; Brunke et al. 2002) or the windless coefficient (Jordan et al. 1999) common in many bulk flux algorithms, including our own previous algorithm (Andreas et al. 2008). Furthermore, this new drag relation naturally predicts the roll off in C_{DN10} with increasing wind speed that hurricane modelers have been seeking.

Using 4000 sets of eddy-covariance measurements made over the open ocean, we first demonstrated that a flux model that predicts only the interfacial fluxes can explain the latent and sensible heat flux data only for wind speeds below 10 m s^{-1}, where spray-mediated fluxes are predicted to be negligible. For higher winds, the measurements show larger fluxes than an interfacial-only model can explain; and the model gets increasingly worse with increasing wind speed. These are the results we expect when spray contributions are ignored.

In contrast, when we included both spray and interfacial contributions in our estimates for the measured fluxes, we could explain for all wind speeds both the magnitude and the wind speed dependence of the measurements by adjusting small, positive constants. In effect, this analysis allowed us to separate the measurements into interfacial and spray contributions.

To complement our fast bulk interfacial flux algorithm, we then fitted these spray contributions with a streamlined microphysical model that yielded a fast spray flux algorithm. In this algorithm, the spray latent heat flux depends on the behavior of droplets that start with 50 μm radius, and the spray sensible heat flux depends on 100 μm droplets. Both fluxes increase as high powers of u_{*B}. Meanwhile, the interfacial fluxes are linear in $u_{*,B}$ in light of our new drag relation.

Three sensitivity plots demonstrate how the respective spray and interfacial fluxes scale differently with state variables and, thus, emphasize that data analysis alone will not produce flux parameterizations that can be reliably extrapolated to environmental conditions outside the range for which they were tuned. Instead, in our view, theoretical models for both the spray and interfacial routes must be tested against data when spray provides a significant transfer route—namely, for 10-m wind speeds above 10–12 m s^{-1}.

We have developed Fortran code for this algorithm that we are willing to share. You can download it at www.nwra.com/resumes/andreas/software.php. An important caveat for using this code is that our analysis of the spray fluxes is intimately tied to our interfacial flux algorithm. You cannot use our spray flux algorithm and another interfacial flux algorithm and expect reliable predictions of the total fluxes. You must use both our interfacial and spray flux algorithms in your application.

8. ACKNOWLEDGMENTS

We thank Ola Persson, Jeff Hare, Chris Fairall, and Bill Otto for the FASTEX data; Nína Petersen and Ian Renfrew for the GFDex data; Janice DeCosmo for advice on working with the HEXOS data; and Emily Moynihan of BlytheVisual for preparing Figure 1. The U.S. Office of Naval Research supported Andreas, Mahrt, and Vickers with award N00014-11-1-0073 and additionally supported Andreas with award N00014-12-C-0290.

9. REFERENCES

Anderson, K., and 20 coauthors, 2004: The RED Experiment: An assessment of boundary layer effects in a trade winds regime on microwave and infrared propagation over the sea. *Bull. Amer. Meteor. Soc.*, **85**, 1355–1365.

Andreas, E. L, 1989: Thermal and size evolution of sea spray droplets. CRREL Rep. 89-11, U.S. Army Cold Regions Research and Engineering Laboratory, Hanover, NH, 37 pp. [NTIS: ADA210484.]

Andreas, E. L, 1990: Time constants for the evolution of sea spray droplets. *Tellus*, **42B**, 481–497.

Andreas, E. L, 1992: Sea spray and the turbulent air-sea heat fluxes. *J. Geophys. Res.*, **97**, 11,429–11,441.

Andreas, E. L, 1995: The temperature of evaporating sea spray droplets. *J. Atmos. Sci.*, **52**, 852–862.

Andreas, E. L, 1996: Reply. *J. Atmos. Sci.*, **53**, 1642–1645.

Andreas, E. L, 2002: A review of the sea spray generation function for the open ocean. *Atmosphere-Ocean Interactions*, Vol. 1, W. Perrie, Ed., WIT Press, Boston, 1–46.

Andreas, E. L, 2004: Spray stress revisited. *J. Phys. Oceanogr.*, **34**, 1429–1440.

Andreas, E. L, 2005: Approximation formulas for the microphysical properties of saline droplets. *Atmos. Res.*, **75**, 323–345.

Andreas, E. L, 2010: Spray-mediated enthalpy flux to the atmosphere and salt flux to the ocean in high winds. *J. Phys. Oceanogr.*, **40**, 608–619.

Andreas, E. L, 2011: Fallacies of the enthalpy transfer coefficient over the ocean in high winds. *J. Atmos. Sci.*, **68**, 1435–1445.

Andreas, E. L, and J. DeCosmo, 1999: Sea spray production and influence on air-sea heat and moisture fluxes over the open ocean. *Air-Sea Exchange: Physics, Chemistry and Dynamics*, G. L. Geernaert, Ed., Kluwer, Dordrecht, 327–362.

Andreas, E. L, and J. DeCosmo, 2002: The signature of sea spray in the HEXOS turbulent heat flux data. *Bound.-Layer Meteor.*, **103**, 303–333.

Andreas, E. L, and K. A. Emanuel, 2001: Effects of sea spray on tropical cyclone intensity. *J. Atmos. Sci.*, **58**, 3741–3751.

Andreas, E. L, and S. Wang, 2007: Predicting significant wave height off the northeast coast of the United States. *Ocean Eng.*, **34**, 1328–1335.

Andreas, E. L, J. B. Edson, E. C. Monahan, M. P. Rouault, and S. D. Smith, 1995: The spray contribution to net evaporation from the sea: A review of recent progress. *Bound.-Layer Meteor.*, **72**, 3–52.

Andreas, E. L, P. O. G. Persson, and J. E. Hare, 2008: A bulk turbulent air-sea flux algorithm for high-wind, spray conditions. *J. Phys. Oceanogr.*, **38**, 1581–1596.

Andreas, E. L, L. Mahrt, and D. Vickers, 2012: A new drag relation for aerodynamically rough flow over the ocean. *J. Atmos. Sci.*, **69**, 2520–2537.

Andreas, E. L, R. E. Jordan, L. Mahrt, and D. Vickers, 2013: Estimating the Bowen ratio over the open and ice-covered ocean. *J. Geophys. Res. Oceans*, **118**, 4334–4345, doi:10.1002/jgrc.20295.

Anguelova, M., R. P. Barber, and J. Wu, 1999: Spume droplets produced by the wind tearing of wave crests. *J. Phys. Oceanogr.*, **29**, 1156–1165.

Bao, J.-W., C. W. Fairall, S. A. Michelson, and L. Bianco, 2011: Parameterization of sea-spray impact on the air-sea momentum and heat fluxes. *Mon. Wea. Rev.*, **139**, 3781–3797.

Barenblatt, G. I., A. J. Chorin, and V. M. Prostokishin, 2005: A note concerning the Lighthill "sandwich model" of tropical cyclones. *Proc. Nat. Acad. Sci.*, **102**, 11,148–11,150.

Bourassa, M. A., D. G. Vincent, and W. L. Wood, 1999: A flux parameterization including the effects of capillary waves and sea state. *J. Atmos. Sci.*, **56**, 1123–1139.

Brunke, M. A., X. Zeng, and S. Anderson, 2002: Uncertainties in sea surface turbulent flux algorithms and data sets. *J. Geophys. Res.*, **107**, 3141, doi:10.1029/2001JC000992.

Chang, H.-R., and R. L. Grossman, 1999: Evaluation of bulk surface flux algorithms for light wind conditions using data from the Coupled Ocean-Atmosphere Response Experiment (COARE). *Quart. J. Roy. Meteor. Soc.*, **125**, 1551–1588.

Chiang, T.-L., C.-R. Wu, and L.-Y. Oey, 2011: Typhoon Kai-Tak: An ocean's perfect storm. *J. Phys. Oceanogr.*, **14**, 221–233.

DeCosmo, J., 1991: Air-sea exchange of momentum, heat and water vapor over whitecap sea states. Ph.D. dissertation, University of Washington, Seattle, 212 pp.

DeCosmo, J., K. B. Katsaros, S. D. Smith, R. J. Anderson, W. A. Oost, K. Bumke, and H. Chadwick, 1996: Air-sea exchange of water vapor and sensible heat: The Humidity Exchange over the Sea (HEXOS) results. *J. Geophys. Res.*, **101**, 12,001–12,016.

de Leeuw. G., E. L Andreas, M. D. Anguelova, C. W. Fairall, E. R. Lewis, C. O'Dowd, M. Schulz, and S. E. Schwartz, 2011: Production flux of sea spray aerosol. *Rev. Geophys.*, **49**, RG2001, doi:10.1029/2010RG000349.

Edson, J., and 28 coauthors, 2007: The Coupled Boundary Layers and Air–Sea Transfer Experiment in low winds. *Bull. Amer. Meteor. Soc.*, **88**, 341–356.

Edson, J. B., V. Jampana, R. A. Weller, S. P. Bigorre, A. J. Plueddemann, C. W. Fairall, S. D. Miller, L. Mahrt, D. Vickers, and H. Hersbach, 2013: On the exchange of momentum over the open ocean. *J. Phys. Oceanogr.*, **43**, 1589–1610.

Fairall, C. W., J. D. Kepert, and G. J. Holland, 1994: The effect of sea spray on surface energy transports over the ocean. *Global Atmos. Ocean Syst.*, **2**, 121–142.

Fairall, C. W., E. F. Bradley, D. P. Rogers, J. B. Edson, and G. S. Young, 1996: Bulk parameterization of air-sea fluxes for Tropical Ocean-Global Atmosphere Coupled-Ocean Atmosphere Response Experiment. *J. Geophys. Res.*, **101**, 3747–3764.

Fairall, C. W., E. F. Bradley, J. E. Hare, A. A. Grachev, and J. B. Edson, 2003: Bulk parameterization of air-sea fluxes: Updates and verification for the COARE algorithm. *J. Climate*, **16**, 571–591.

Fairall, C. W., M. L. Banner, W. L. Peirson, W. Asher, and R. P. Morison, 2009: Investigation of the physical scaling of sea spray spume droplet production. *J. Geophys. Res.*, **114**, C10001, doi:10.1029/2008JC004918.

Foreman, R. J., and S. Emeis, 2010: Revisiting the definition of the drag coefficient in the marine atmospheric boundary layer. *J. Phys. Oceanogr.*, **40**, 2325–2332.

Garratt, J. R., 1992: *The Atmospheric Boundary Layer*. Cambridge University Press, Cambridge, UK, 316 pp.

Grachev, A. A., E. L Andreas, C. W. Fairall, P. S. Guest, and P. O. G. Persson, 2007: SHEBA flux-profile relationships in the stable atmospheric boundary layer. *Bound.-Layer Meteor.*, **124**, 315–333.

Grant, A. L. M., and P. Hignett, 1998: Aircraft observations of the surface energy balance in TOGA-COARE. *Quart. J. Roy. Meteor. Soc.*, **124**, 101–122.

Jarosz, E., D. A. Mitchell, D. W. Wang, and W. J. Teague, 2007: Bottom-up determination of air-sea momentum exchange under a major tropical cyclone. *Science*, **315**, 1707–1709.

Jordan, R. E., E. L Andreas, and A. P. Makshtas, 1999: The heat budget of snow-covered sea ice at North Pole 4. *J. Geophys. Res.*, **104**, 7785–7806.

Kepert, J., C. Fairall, and J.-W. Bao, 1999: Modelling the interaction between the atmospheric boundary layer and evaporating sea spray droplets. *Air-Sea Exchange: Physics, Chemistry and Dynamics*, G. L. Geernaert, Ed., Kluwer, Dordrecht, 363–409.

Kudryavtsev, V. N., 2006: On the effect of sea drops on the atmospheric boundary layer. *J. Geophys. Res.*, **111**, C07020, doi:10.1029/2005JC002970.

Kudryavtsev, V. N., and V. K. Makin, 2011: Impact of ocean spray on the dynamics of the marine atmospheric boundary layer. *Bound.-Layer Meteor.*, **140**, 383–410.

Lee, C.-Y., and S. S. Chen, 2012: Symmetric and asymmetric structures of hurricane boundary layer in coupled atmosphere-wave-ocean models and observations. *J. Atmos. Sci.*, **69**, 3576–3594.

Lighthill, J., 1999: Ocean spray and the thermodynamics of tropical cyclones. *J. Eng. Math.*, **35**, 11–42.

Liu, W. T., K. B. Katsaros, and J. A. Businger, 1979: Bulk parameterization of air-sea exchanges of heat and water vapor including the molecular constraints at the interface. *J. Atmos. Sci.*, **36**, 1722–1735.

Lykossov, V. N., 2001: Atmospheric and oceanic boundary layer physics. *Wind Stress over the Ocean*, I. S. F. Jones and Y. Toba, Eds., Cambridge University Press, Cambridge, UK, 54–81.

Mahrt, L., and D. Khelif, 2010: Heat fluxes over weak SST heterogeneity. *J. Geophys. Res.*, **115**, D11103, doi:10.1029/2009JD013161.

Mahrt, L., D. Vickers, P. Frederickson, K. Davidson, and A.-S. Smedman, 2003: Sea-surface aerodynamic roughness. *J. Geophys. Res.*, **108**, 3171, doi:10.1029/2002JC001383.

Mahrt, L., D. Vickers, E. L Andreas, and D. Khelif, 2012: Sensible heat flux in near-neutral conditions over the sea. *J. Phys. Oceanogr.*, **42**, 1134–1142.

Montgomery, M. T., R. K. Smith, and S. V. Nguyen, 2010: Sensitivity of tropical cyclone models to the surface drag coefficient. *Quart. J. Roy. Meteor. Soc.*, **136**, 1945–1953.

Moon, I.-J., I. Ginis, T. Hara, and B. Thomas, 2007: A physics-based parameterization of air-sea momentum flux at high wind speeds and its impact on hurricane intensity predictions. *Mon. Wea. Rev.*, **135**, 2869–2878.

Mueller, J. A., and F. Veron, 2009a: Nonlinear formulation of the bulk surface stress over breaking waves: Feedback mechanisms from air-flow separation. *Bound.-Layer Meteor.*, **130**, 117–134.

Mueller, J. A., and F. Veron, 2009b: A sea state dependent spume generation function. *J. Phys. Oceanogr.*, **39**, 2363–2372.

Oncley, S. P., C. A. Friehe, J. C. Larue, J. A. Businger, E. C. Itsweire, and S. S. Chang, 1996: Surface-layer fluxes, profiles, and turbulence measurements over uniform terrain under near-neutral conditions. *J. Atmos. Sci.*, **53**, 1029–1044.

Paulson, C. A., 1970: The mathematical representation of wind speed and temperature profiles in the unstable atmospheric surface layer. *J. Appl. Meteor.*, **9**, 857–861.

Perrie, W., E. L Andreas, W. Zhang, W. Li, J. Gyakum, and R. McTaggart-Cowan, 2005: Sea spray impacts on intensifying midlatitude cyclones. *J. Atmos. Sci.*, **62**, 1867–1883.

Persson, P. O. G., J. E. Hare, C. W. Fairall, and W. D. Otto, 2005: Air-sea interaction processes in warm and cold sectors of extratropical cyclonic storms observed during FASTEX. *Quart. J. Roy. Meteor. Soc.*, **131**, 877–912.

Petersen, G. N., and I. A. Renfrew, 2009: Aircraft-based observations of air-sea fluxes over Denmark Strait and the Irminger Sea during high wind speed conditions. *Quart. J. Roy. Meteor. Soc.*, **135**, 2030–2045.

Pielke, R. A., and T. J. Lee, 1991: Influence of sea spray and rainfall on the surface wind profile during conditions of strong winds. *Bound.-Layer Meteor.*, **55**, 305–308.

Pruppacher, H. R., and J. D. Klett, 2010: *Microphysics of Clouds and Precipitation*, 2nd Revised Edition. Springer, Dordrecht, 954 pp.

Richter, D. H., and P. P. Sullivan, 2013: Sea surface drag and the role of spray. *Geophys. Res. Lett.*, **40**, 656–660, doi:10.1002/grl.50163.

Rogers, R., and 22 coauthors, 2013: NOAA's hurricane Intensity Forecasting Experiment. *Bull. Amer. Meteor. Soc.*, **94**, 859–882.

Romero, L., and W. K. Melville, 2010: Airborne observations of fetch-limited waves in the Gulf of Tehuantepec. *J. Phys. Oceanogr.*, **40**, 441–465.

Sanford, T. B., J. F. Price, J. B. Girton, and D. C. Webb, 2007: Highly resolved observations and simulations of the ocean response to a hurricane. *Geophys. Res. Lett.*, **34**, L13604, doi:10.1029/2007GL029679.

Shpund, J., M. Pinsky, and A. Khain, 2011: Microphysical structure of the marine boundary layer under strong wind and spray formation as seen from simulations using a 2D explicit microphysical model. Part I: The impact of large eddies. *J. Atmos. Sci.*, **68**, 2366–2384.

Shpund, J., J. A. Zhang, M. Pinsky, and A. Khain, 2012: Microphysical structure of the marine boundary layer under strong wind and spray formation as seen from simulations using a 2D explicit microphysical model. Part II: The role of sea spray. *J. Atmos. Sci.*, **69**, 3501–3514.

Smith, S. D., 1988: Coefficients for sea surface wind stress, heat flux, and wind profiles as a function of wind speed and temperature. *J. Geophys. Res.*, **93**, 15,467–15,472.

Sun, J., J. F. Howell, S. K. Esbensen, L. Mahrt, C. M. Greb, R. Grossman, and M. A. LeMone, 1996: Scale dependence of air-sea fluxes over the Western Equatorial Pacific. *J. Atmos. Sci.*, **53**, 2997–3012.

Sun, J., D. Vandemark, L. Mahrt, D. Vickers, T. Crawford, and C. Vogel, 2001: Momentum transfer over the coastal zone. *J. Geophys. Res.*, **106**, 12,437–12,448.

Tang, B., and K. Emanuel, 2012: Sensitivity of tropical cyclone intensity to ventilation in an axisymmetric model. *J. Atmos. Sci.*, **69**, 2394–2413.

Van Eijk, A. M. J., B. S. Tranchant, and P. G. Mestayer, 2001: SeaCluse: Numerical simulation of evaporating sea spray droplets. *J. Geophys. Res.*, **106**, 2573–2588.

Veron, F., C. Hopkins, E. L. Harrison, and J. A. Mueller, 2012: Sea spray spume droplet production in high wind speeds. *Geophys. Res. Lett.*, **39**, L16602, doi:10.1029/2012GL052603.

Vickers, D., and S. K. Esbensen, 1998: Subgrid surface fluxes in fair weather conditions during TOGA COARE: Observational estimates and parameterization. *Mon. Wea. Rev.*, **126**, 620–633.

Vickers, D., L. Mahrt, and E. L Andreas, 2013: Estimates of the 10-m neutral sea surface drag coefficient from aircraft eddy-covariance measurements. *J. Phys. Oceanogr.*, **43**, 301–310.